Provided for non-commercial research and education use.
Not for reproduction, distribution or commercial use.

This article appeared in a journal published by Elsevier. The attached copy is furnished to the author for internal non-commercial research and education use, including for instruction at the authors institution and sharing with colleagues.

Other uses, including reproduction and distribution, or selling or licensing copies, or posting to personal, institutional or third party websites are prohibited.

In most cases authors are permitted to post their version of the article (e.g. in Word or Tex form) to their personal website or institutional repository. Authors requiring further information regarding Elsevier's archiving and manuscript policies are encouraged to visit:

http://www.elsevier.com/copyright

Author's personal copy

Applied Surface Science 255 (2008) 3097–3103

Contents lists available at ScienceDirect

Applied Surface Science

journal homepage: www.elsevier.com/locate/apsusc

Hybrid atomistic-macroscale modeling of long-time phase change in nanosecond laser–material interaction

Lijun Zhang [a], Xinwei Wang [b,*]

[a] Department of Mechanical Engineering, N104 Walter Scott Engineering Center, The University of Nebraska-Lincoln, Lincoln, NE 68588-0656, United States
[b] Department of Mechanical Engineering, 2010 H.M. Black Engineering Building, Iowa State University, Ames, IA 50011-2161, United States

ARTICLE INFO

Article history:
Received 2 May 2008
Received in revised form 23 August 2008
Accepted 29 August 2008
Available online 6 September 2008

PACS:
31.15.at
79.20.Ds
83.10.Tv

Keywords:
Atomistic-macroscale modeling
Nanosecond laser–material interaction
Phase change

ABSTRACT

In this work, large-scale hybrid atomistic-macroscale simulation is performed to study the long-time material behavior in nanosecond laser–material interaction. Different phase change phenomena are studied, including solid–liquid interface speed, temperature, maximum melting depth, and ablation rate. Full solidification/epitaxial re-growth is observed within 60 ns for the laser fluence of 5 J/m^2. Strong fluctuation is observed at the solid–liquid interface and surface of the molten pool. No visible superheating is observed at the solid–liquid interface. For the laser fluences studied in this work, an almost linear relationship is observed between the ablation yield and the laser fluence, indicating weak phase explosion.

© 2008 Elsevier B.V. All rights reserved.

1. Introduction

In the last decade, laser–material interaction has attracted significant attention due to the wide spectrum of applications of lasers in material processing, nanomaterial synthesis, laser-assisted machining, and surface modification. Understanding the underlying physics in laser–material interaction still remains quite challenging due to the great complexity of the process. It involves coupled photo-material interaction, material structural change, extremely strong stress generation and propagation, heating, as well as phase change and explosion. To date, extensive theoretical and experimental investigations are still in progress to obtain in-depth knowledge of the physical processes involved in laser–material interaction.

Molecular dynamics (MD) simulation, which tracks the movement of individual atoms, provides the great capability of studying the coupled physical phenomena in laser–material interaction. To obtain physically reasonable results, systems consisting of tens of thousands, millions, or more atoms are usually required in MD simulation. This significantly limits the time scale of MD simulation. Reported MD simulation of laser–material interaction is largely limited to picosecond and femtosecond lasers. For this type of laser–material interaction, the short heating time of the laser makes it feasible to conduct atomistic modeling. For nanosecond laser–material interaction, very few reports are available about the atomic-level understanding of the process. The biggest challenge faced by this type of modeling is time—the physical process (~60 ns) requires months to model by using moderate computer clusters. In addition, in nanosecond laser–material interaction, the heat transfer and stress wave propagation in the solid part could extend to a significant length, requiring a large physical domain or special physical and modeling treatment to capture/account for these long-time material behaviors. Atomistic level understanding about the melting, phase explosion, as well as the molten nanoparticle formation in nanosecond laser–material interaction, is crucial for high-degree control and optimization of the process.

MD simulations have been used for years to study laser–material interactions. Shibahara and Kotake [1] studied the interaction between metallic atoms and a laser beam in a system consisting of 13 or fewer atoms. Their work focused on the structural change of metallic atoms due to laser beam absorption. Häkkinen and Landman [2] studied dynamics of superheating, melting, and annealing at the Cu surface induced by laser beam irradiation.

* Corresponding author. Tel.: +1 515 294 2085; fax: +1 515 294 3261.
E-mail address: xwang3@iastate.edu (X. Wang).

0169-4332/$ – see front matter © 2008 Elsevier B.V. All rights reserved.
doi:10.1016/j.apsusc.2008.08.098

Author's personal copy

Kotake and Kuroki [3] studied laser ablation of a small dielectric system. In their work, laser beam absorption was simulated by exciting the potential energy of atoms. Applying the same laser beam absorption approach, Herrmann et al. [4] investigated laser ablation of a silicon crystal containing approximately 23,000 atoms. Zhigilei et al. [5,6] studied laser-induced ablation of organic solids using the breathing sphere model, which approximated laser irradiation by exciting the molecular vibration. Their work revealed a number of physical phenomena in ps laser organic material interaction, which can be found in a recent paper and the references cited inside [7]. For laser–material interaction, different techniques have been employed to consider thermal transport by electrons, which cannot be accounted for within classical MD schemes. Examples include forced heat conduction between atoms [8] and combined atomistic-continuum modeling [9–11]. The mechanical wave in laser–material interaction in a large system was studied by Etcheverry and Mesaros [12]. In recent years, thermal transport, phase change, thermal stress development and propagation, and nanoparticle formation in laser–material interaction have been extensively investigated. Xu et al. [13] investigated femtosecond laser ablation of copper with the emphasis on the understanding of the mechanism of phase change during laser ablation and studied non-equilibrium phase change in metal induced by nanosecond pulsed laser irradiation [14]. The dynamics of plume formation and parameters of the ejected clusters in picosecond laser ablation has been studied by Zhigilei [15] using large-scale molecular dynamics simulations. Their results showed the phase explosion of overheated material led to the formation of a foamy transient structure of interconnected liquid regions that subsequently decomposed into a mixture of liquid droplets, gas phase molecules and small clusters. The cooling rates and recrystallization kinetics, the effect of pressure relaxation on the mechanisms, and the channels of energy redistribution, in picosecond laser ablation, have been investigated by Zhigilei [16–18].

In this work, large-scale hybrid atomistic-macroscale simulation is conducted to study the long-time (~60 ns) phase change behavior in nanosecond laser–material interaction. To make the computation efficient and feasible, parallel algorithm is applied. Additionally, dynamic work load distribution among computing nodes is designed and used during parallel computation to significantly improve the computational efficiency. The research focuses on the phase change, material removal, structural evolution, and effect of the laser fluence on material ablation. The methodologies of hybrid atomistic-macroscale modeling are described in Section 2. The atomistic level pictures of the phase change process are presented and analyzed in Section 3.

2. Methodologies of hybrid atomistic-macroscale modeling

Fig. 1(a) shows how the computational domain is designed for hybrid atomistic-macroscale modeling. The whole physical space is divided into two domains. Materials in Domain I are subjected to nanosecond laser heating and experience intensive structural change. MD simulation is conducted to model the material behavior in Domain I. Materials in Domain II only experience heat conduction. Therefore, the finite difference (FD) method is used to model the heat transfer in Domain II. The one-dimensional heat conduction equation is solved in Domain II for heat transfer. The thermophysical properties (specific heat and thermal conductivity) of the material are temperature dependent and updated in the FD simulation every time step. Periodical boundary conditions are used along the x and z directions shown in Fig. 1. In the simulation, the FD calculation and MD simulation are coupled and conducted simultaneously. In general, the MD domain should be designed to be much longer (in laser incidence direction)

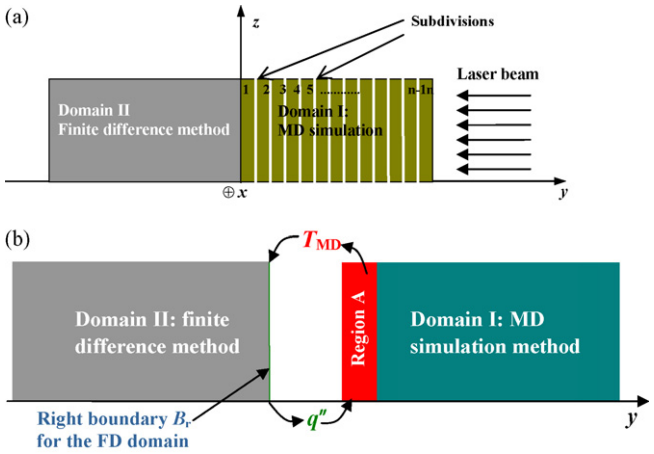

Fig. 1. (a) Schematic of the computational domain; (b) schematic for treatment of the interface between the MD and FD domains. (For interpretation of the references to colour in the citation of this figure, the reader is referred to the web version of the article.)

than the laser melting depth. The thickness of the FD domain should be larger than the thermal diffusion length in the target within the time of simulation.

At the interface between Domains I and II, the temperature and heat flux are continuous. In Domain I, one small region is selected on the left boundary [Region A shown in Fig. 1(b)]. The thickness of the boundary region is equal to the cut-off distance of the interaction potential used in the MD region with the value of 2.5σ (σ: equilibrium atomic separation in the Lennard–Jones potential for describing the material). At each time step, the temperature of this region will be calculated as T_{MD}. This temperature is used to provide the boundary condition [boundary B_r indicated in Fig. 1(b)] for the FD calculation in Domain II in the next time step calculation. At the same time step, the heat flux (q'') at the interface is calculated based on the temperature gradient at the boundary B_r in domain II. This temperature gradient is determined by the temperature distribution in Domain II by using the FD method. It is understandable this heat flux should come from the MD domain. At each time step, an energy of $\Delta E = \delta t\, q'' A$ will be taken away from Region A (red area) in Domain I. Here δt is the time step in MD simulation and A is the cross-sectional area of Domain I in the y direction. This energy subtraction can be achieved by adjusting the kinetic energy of atoms in Region A.

When a laser pulse irradiates the material (Domain I) from the right side, a strong stress wave will emerge in the material and propagate to the left side. When this strong stress wave reaches the left boundary of the MD domain, two phenomena could happen. One is that the strong tensile stress can tear the material near the left boundary of the MD domain, inducing unrealistic material damage. The other phenomenon is that the stress wave will be reflected at the left boundary, and then propagate to the right boundary. When this reflected stress reaches the molten region, it may introduce strong unexpected disturbance to the liquid–vapor phase change. In this paper, a special boundary treatment is exercised at the left boundary [Region A shown in Fig. 1(b)] to eliminate the above phenomena. One force that mimics the force induced by the stress wave propagating in the y direction will be applied to atoms in Region A. This force takes the form of [19]

$$F_s = -\rho v c \cdot \frac{A}{N}, \tag{1}$$

where ρ is the density of the target in Region A, v the average velocity in the y direction for atoms within Region A, c the speed of

Author's personal copy

the stress wave in the y direction, and N is the number of atoms within Region A. In our extensive MD simulations, the above stress boundary treatment proved to work very well in terms of eliminating stress wave reflection and avoiding undesired material damage in the boundary region. Without the no-reflective boundary condition, like frigid or free boundary conditions, complete reflection of the stress wave occurred and the compressive pressure wave transformed into a tensile stress wave in the boundary region. Significant damage near the boundary region contributed to the material separation and ejection from the interconnected computational cell, resulting in fewer atoms in the computational cell. Under such condition, the computation is always interrupted by the damage. On the contrary, with the no-reflective boundary condition, the compressive pressure is absorbed by the no-reflective boundary by 95%.

In this work, parallel computation is used for the MD simulation. The whole physical space in Domain I is divided into subdivisions, and each sub-division is assigned to a computing node as shown in Fig. 1(a). Each computing node is responsible for the MD simulation of one sub-division. The information exchange among sub-divisions (computing nodes) is realized through integrating MPICH into MD programs. In order to effectively utilize the power of the computer cluster that communicates over a network, the computation load on each node is dynamically monitored and re-distributed with a certain time interval. This work load re-distribution involves re-dividing the computational space in Domain I. The size of the subdivision calculated by each node will be controlled to make sure that all the computing nodes have nearly the same number of atoms for modeling.

The laser beam is absorbed exponentially with an optical absorption depth τ following the formula $dI/dy = I/\tau$ using the coordinate shown in Fig. 1. The MD domain is divided into many layers along the y direction whose thickness δy is around the cutoff distance in force calculation. Within each time step, the original laser beam irradiating the target surface is E_0 (in the unit of J). The energy absorbed inside the first layer is $\Delta E = E_0\{1 - \exp[-\delta y/(\tau\rho_0/\rho)]\}$, where ρ_0 and ρ are the bulk density and true density of the target, respectively. Laser beam absorption in the cell is achieved by exciting the kinetic energy of atoms, which is fulfilled by scaling the velocities of atoms with an appropriate factor. Details of laser beam absorption have been discussed in our previous work [21–25].

3. Results and discussion

In this work, a freestanding film of argon is irradiated by a nanosecond laser. The profile of the laser intensity against time is shown in Fig. 5(b) when discussing the melting speed. The full-width at half maximum (FWHM) of the laser pulse is 11.3 ns with its peak intensity located at 9.5 ns. The Lennard–Jones (LJ) well depth parameter (ε) and equilibrium separation (σ) takes 1.653×10^{-21} J and 3.406 Å, respectively. The half-step leap-frog scheme is used [20] in this work with a time step of 25 fs. The interaction between atoms is neglected when their distance is beyond the cutoff distance r_c, which is 2.5σ. In this work, the distribution of the optical field over the cross-section of the target is uniform, and the laser intensity variation with time takes the form measured for a Nd:YLF laser. An artificial absorption depth of 15 nm is employed in the simulation. When the laser beam goes through every cell along the y direction, the atoms in each cell absorb part of the energy with considering the exponential absorption of the laser beam in the incident direction. Absorption of laser in the sample is achieved by only exciting the kinetic energy of atoms while keeping their momentum conserved. Details of the computational principles and laser energy absorption are described in our previous work [21–25].

Before applying laser heating, the simulation is run for 100 ps (4000 steps), during which the velocity of atoms is scaled to make the sample to reach 50 K gradually. After this velocity scaling, the sample is simulated for another 100 ps (4000 steps) to eliminate the disturbance introduced by velocity scaling. The sample measures 32.4 nm in the x direction, 2.7 nm in the z direction and 341 nm in the y direction. A total of 756,000 atoms are simulated for this case. It takes about 0.8 s to finish one time step (25 fs) calculation by using 36 computing cores. The entire 60 ns calculation takes about 22 days to finish by using 36 computing cores. Additionally, a similar computation (case 2) is performed on another computer cluster. This computation is intended to check the uncertainty and repeatability of MD simulation for predicting material behavior for a much prolonged time. All parameters and target size are identical except that case 2 takes a y direction size of 355 nm. The total number of atoms is 776,000 for case 2.

In this work, the distribution and evolution of the ejected plume in a large space and time scale is one of our research focuses. Since the development of the plume is slow and time is long (up to 60 ns), the size of the ejected plume in the y direction is continually changing and becomes very long. In order to catch the size precisely while saving the computational cost, we use a dynamic domain scheme in the y direction to expedite the calculation. With the moving of atoms at each time step, the maximum length in the y direction is evaluated. The size of the computational domain in the y direction is dynamically increased to just contain all the atoms in space. According to this dynamic domain algorithm, the expansion and development of the ejected plume are exactly recorded in the calculation. The length in the y direction by the end of the MD simulation at the laser fluence of 20 J/m^2 is up to 113 μm.

3.1. Snapshots of atomic positions

In this section, the snapshots of atomic positions are provided first to give a general picture of the atomic behavior in nanosecond laser–material interaction. In general, the snapshots at all calculated laser fluencies including 5, 10, 15, and 20 J/m^2 share the same visual pictures of the active process occurring during laser irradiation, such as the occurrence of melting, vaporization, recrystallization, followed by density fluctuation and vapor expansion. However, at the laser fluence of 20 J/m^2, it is noticed that the phenomena of the ejected material are more intense and show appreciable difference. Fig. 2 shows the snapshots of atomic positions in an x–y plane at 20 J/m^2. In these figures, each dot represents an atom. Since the range in the y direction is too large, only the interesting range (306.5–1021.8 nm) is plotted. The snapshots at 8 ns (close to the peak laser intensity time), 10, 11, 12, 13 and 15 ns are illustrated. Snap shots after 15 ns show gradual change of the vapor in space similar to that at 15 ns, and are not plotted here. At 10 ns, there are two apparent distorted parts (due to the compressed coordinates, only two barely visible spots are shown in the figure) in the subsurface region which look like a layer is formed and separated from the surface. The inset at 10 ns shows the clear picture about how the material is separated from the surface region. The voids in the sub-surface region and the molten material in the surface region cannot hold as an integral part. The layer-like material is ejected from the surface (11 ns). After it separates from the molten region, it is gradually decomposed into small parts of liquid or gas-phase atoms. Compared with the picosecond laser–material interaction we studied before [23], under the same laser fluence input the nanosecond laser–material interaction is much less intense and shows limited nucleation and bubble formation. It is seen from Fig. 2 that the number of large particles is quite limited. Most of the

Author's personal copy

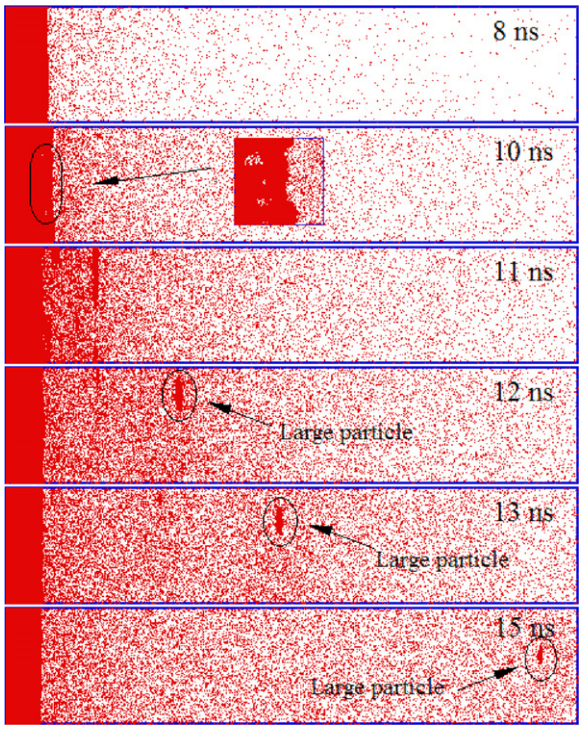

Fig. 2. Snapshots of atomic positions with a laser fluence of 20 J/m^2. Vertical coordinate: 0–32.4 nm, horizontal coordinate: 306.5–1021.8 nm. The inset at 10 ns shows the enlarged region of nucleation and ablation. The atomic positions before 8 ns and after 15 ns are not shown since the process is very slow and the atoms do not have significant position change.

ablation material comes out as gas or small clusters. A large particle is observed in the ablation plume which is marked in the snapshot at 12, 13 and 15 ns in Fig. 2. Due to the cluster–cluster collision, evaporation and condensation, the laminated material separated from the surface breaks up and splits into large particles. The size of the large particle becomes smaller during its movement in space. The moving speed of the large particle at 13 ns is around 130 and 165 m/s at 15 ns. Such acceleration of the particle could be due to the pressure gradient in space, which is largely induced by the higher vapor density in the area closer to the molten region.

3.2. Melting and vaporization

Before studying the melting and vaporization process, we calculate the melting temperature of Ar in vacuum and use this value as a reference to study the temperature evolution of the sample under laser irradiation. A sample with a smaller size, 2.7 nm in the x direction, 9.7 nm in the y direction, and 2.7 nm in the z direction, is heated in MD simulation. Then the sample is equilibrated for 100 ps. When the structure of the crystal becomes random, this means melting starts, the local temperature at that time can be reasonably regarded as the melting temperature. Our MD simulation reveals that the melting temperature is about 73 K under the vacuum condition for Ar. This number is a little lower than melting point of 83.8 K reported in literature under atmospheric pressure condition.

Fig. 3 shows the solid–liquid interface temperature, liquid surface temperature, and the average temperature of the molten region at laser fluences of 5, 10, 15 and 20 J/m^2. The solid–liquid interface temperature is around the calculated melting point of 73 K, and no superheating is observed at this interface. The surface temperature rises quickly at the beginning of the laser irradiation. The peak average temperature of the molten region is 100 K at

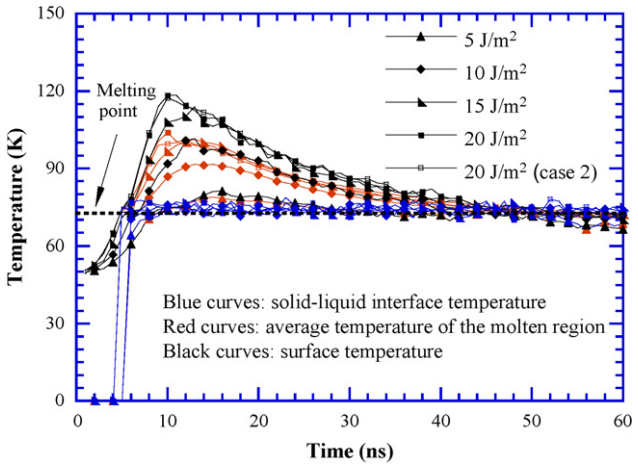

Fig. 3. Evolution of the surface temperature, liquid temperature and solid–liquid interface temperature under different laser fluences.

11 ns (20 J/m^2), 101 K at 13 ns (15 J/m^2), 91 K at 13 ns (10 J/m^2) and 78 K at 15 ns (5 J/m^2). A close observation of Fig. 3 reveals that the surface temperature at laser fluence of 5 J/m^2 gradually increases during laser heating and the peak of the temperature is close to 80 K, which is higher than the melting point of 73 K. Superheating in the surface region happens. Compared to the surface temperature at low fluence of 5 J/m^2, the surface temperature at laser fluence of 20 J/m^2 significantly increases and the peak value is 120 K, which is close to 0.8 T_c (T_c = 150.8 K).

The other important phenomenon in laser–material interaction is the solidification driven by heat conduction in the solid region. Knowledge of the rate of solidification is important to understand how melting and solidification take place. One direct way to measure the rate of solidification is how fast the volume of the liquid decreases with time. To characterize the volume reduction rate of the liquid, criteria have to be established to distinguish the liquid and solid. In this work, a simple definition of the crystallinity is designed as [21]

$$\Phi(r_{i,y}) = \frac{1}{N}\left|\sum_i e^{j2\pi\cdot 2r_{i,y}/\lambda}\right| \quad (2)$$

where $r_{i,y}$ is the y coordinate of atom i, N the number of atoms within the domain of interest, and λ is the light wavelength. In this work, λ takes the value of the lattice constant a. In Eq. (2), $2r_{i,y}$ is the distance one light travels when it originates from $y = 0$, reflected by the atom i at the location of $r_{i,y}$, and then returns to the original location $y = 0$. If atoms are regularly distributed in space with their spacing in the y direction equal to $na/2$, the function $\Phi(r_{i,y})$ will be equal to 1. In liquid, the function $\Phi(r_{i,y})$ will be much less than 1.

Fig. 4 shows the crystallinity function $\Phi(r_{i,y})$ at t = 30 ns with a laser fluence of 20 J/m^2. In the solid region, $\Phi(r_{i,y})$ is around 0.9, meaning atoms are regularly distributed in space due to the sound regularity of crystal structure. On the other hand, in the liquid region, atoms are randomly distributed in space, and the function $\Phi(r_{i,y})$ is less than 0.1. The inset in Fig. 4 shows the crystallinity function works well to distinguish the liquid and solid. As marked by arrow in Fig. 4, at the solid–liquid interface, $\Phi(r_{i,y})$ quickly drops from 0.8 to 0.05 from the solid to liquid side. At the solid–liquid interface, the value of $\Phi(r_{i,y})$ is around 0.5. In this work, 0.5 is used as the criterion to identify the solid–liquid interface.

Fig. 5(a) shows the evolution of the solid–liquid interface determined using the criterion: $\Phi(r_{i,y}) < 0.5$ for liquid and $\Phi(r_{i,y}) > 0.5$ for solid. At the early stage, the position of the

Author's personal copy

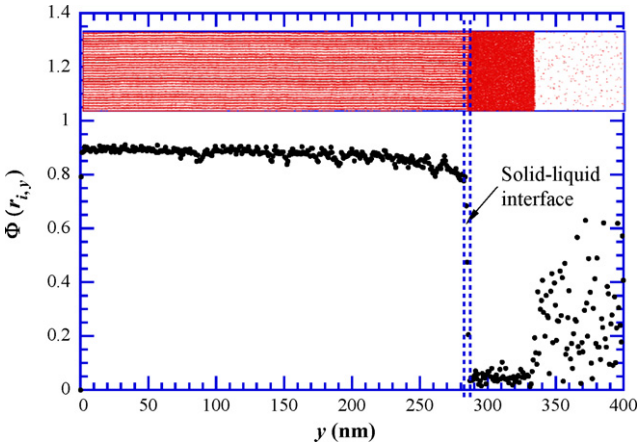

Fig. 4. The distribution of crystallinity function $\Phi(r_{i,y})$ at 30 ns at laser fluence of 20 J/m^2. The inset shows the atomic positions at 30 ns.

solid–liquid interface is a little higher than the original target surface due to thermal expansion. Based on the curve at 20 J/m^2, the melting depth is up to 56 nm and the solidification starts at 35 ns. At 10 and 15 J/m^2, the melting depth is 43 and 51 nm and the solidification starts at 29 and 31 ns, respectively. At 5 J/m^2, it can be observed that solidification is fully finalized within 60 ns. The melting depth is only 21 nm due to the low laser energy input. A general conclusion drawn from Fig. 5(a) is that when the laser fluence is higher, the melting stops much later and goes deeper. A comparison between the two cases of 20 J/m^2 is performed. The curves of the two cases are almost identical. It needs to be pointed out these two cases have different numbers of atoms in the computational domain, they are calculated using different computer clusters (one is Windows cluster, and the other one is Linux cluster), and different random initial atomic velocities are used. Our result analysis shows excellent repeatability of the calculation. Negligible statistical uncertainty is observed.

To have an in-depth understanding of the full solidification/recrystallization at 5 J/m^2 laser fluence, Fig. 6 shows the snapshots of atomic positions in an x–y plane and demonstrates the melting and full solidification/epitaxial re-growth of the Ar crystal. It is observed that the solid–liquid interface is nonuniform although the computation features uniform laser heating and periodical boundary conditions in the x and z directions. This is because the relatively slow heating gives enough time for the molten material to fluctuate. Therefore, the molten pool on the top of the solid has quite strong movement due to non-uniformity of surface tension and fluctuation of the temperature. In addition to the solid–liquid interface, the surface of the molten pool is also fluctuating strongly. Such fluctuation leads to a final rough solid surface (50 ns). In post data processing, we plot the average velocity vector of small regions 1.7 nm × 1.7 nm ($x \times z$). It is found that the velocity in the x and z directions is very small, does not show appreciable macro-movement. The velocity in the z direction (laser incidence direction) is small in the molten and solid parts. At the surface of the molten region, a velocity oscillation in the order of a few m/s is observed.

Fig. 5(b) shows the local speed of the solid–liquid interface versus time at different laser fluences. At the initial stage of melting, the velocity is negative because of the surface thermal expansion. After then, the velocity increases significantly due to the strong laser heating. The peak velocity is proportional to the value of the laser fluence. In Fig. 5(b), the melting and solidification regions are distinguished based on the velocity of the solid–liquid interface (negative velocity for solidification). It is obvious what

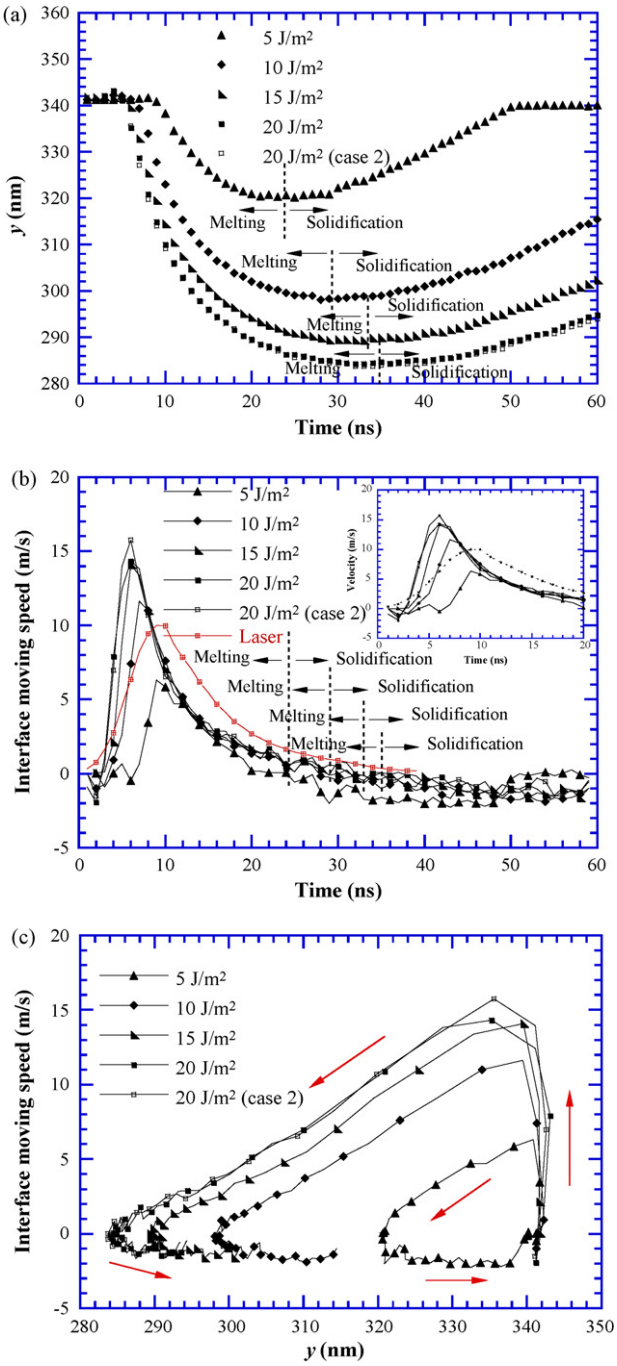

Fig. 5. (a) Location of the solid–liquid interface versus time at different laser fluences; (b) evolution of the local moving speed of the solid–liquid interface; (c) interface moving speed versus the height of the solid–liquid interface. The arrows in (c) show the moving direction of the interface against time.

when the laser fluence is higher, the solidification starts later and the solidification rate is lower. Fig. 5(c) shows how the melting speed changes with the solid–liquid interface location. This figure is very helpful in terms of picturing the melting and solidification process. A close investigation of Fig. 5(c) shows that the interface moving speed has an almost linear relation with respect to the height of the solid–liquid interface. Fig. 5(c) shows how the solid–liquid interface moving speed varies with the interface location. The arrows in the figure show moving direction of the interface against time. It is observed that at the peak melting speed, a very

Author's personal copy

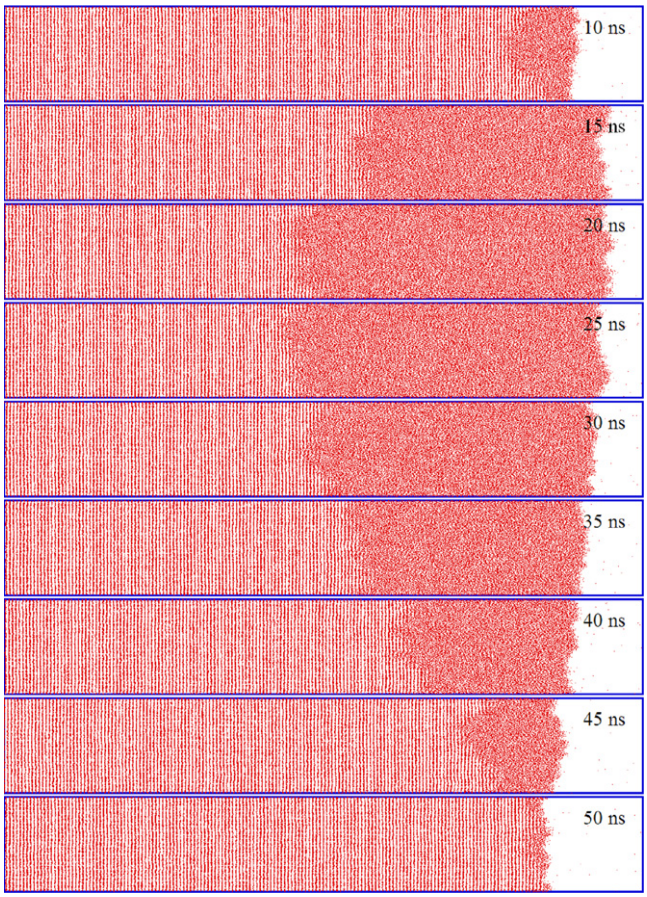

Fig. 6. Melting and full solidification/epitaxial regrowth of Ar crystal under laser fluence of 5 J/m^2. Vertical coordinate: 0–32.4 nm; horizontal coordinate: 306.5–357.6 nm.

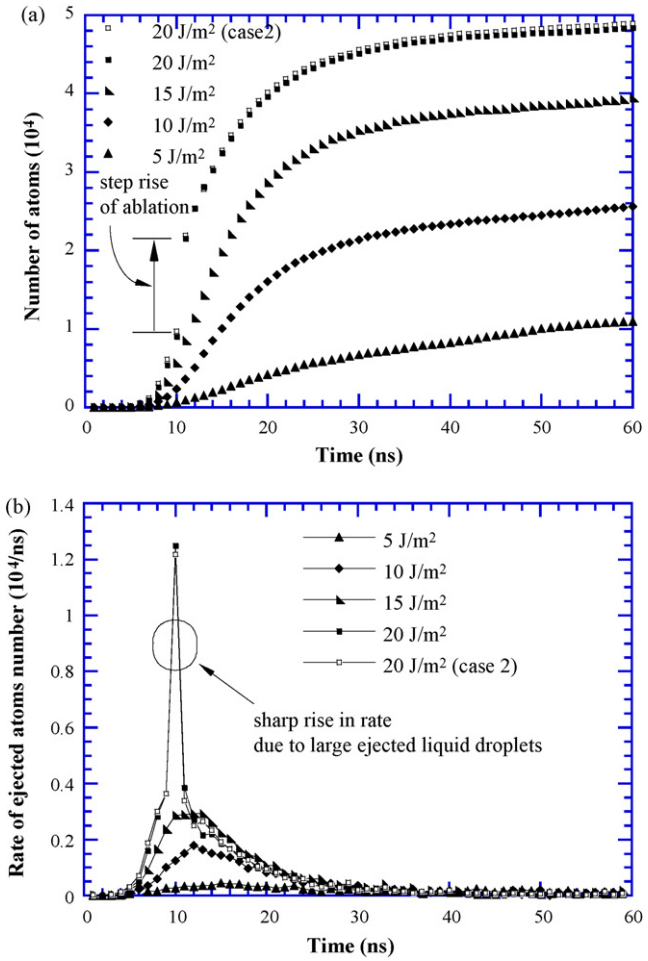

Fig. 7. (a) The mass removal versus time at different laser fluences; (b) evolution of the material ablation rate at different laser fluences.

small amount of material is melted. The closed loop for the 5 J/m^2 case confirms that solidification completes during our computational time. In fact it is seen that when the melting speed reaches its peak velocity, the laser energy does not reach the peak value yet (except the 5 J/m^2 case). The observed decay of the melting speed probably is due to two reasons. One reason is that the large energy (latent heat) needed for melting will slow down the heating and reduce the melting speed. The other reason is that once a large temperature gradient is established in the material, the heat conduction will transfer a large amount of energy from the solid–liquid interface, leading to reduced melting speed. Fig. 5(b) shows that once the melting speed (v_m) reaches the peak value, its decay can be approximated by an exponential function of $v_m \sim e^{-\alpha t}$. Integrating this function from 0 to t leads to the melting depth in the form of $x \sim (1 - e^{-\alpha t})/\alpha$. It is not difficult to find that $v_m \sim (1 - x/\alpha)$. This explains the nearly linear relationship between the location of the solid–liquid interface and its moving speed observed in Fig. 5(c) in the melting slowing-down region.

3.3. Material removal

The amount of material removal induced by the laser fluence is an important part of laser desorption/ablation process. Fig. 7(a) shows the ejected plume evolution at different laser fluences. Since the starting time and position for the ejected plume vary for different laser fluences, we use a dynamic criterion to capture the quantity of the ejected plume. The density of the ablation material is a simple but important parameter to distinguish the ablation material. For the material ablated out, its density is much smaller than those of the solid or molten materials which are not separated from the surface region. So the ejected plume is determined by using a proper value of the density. Normally in each computational layer, solid or molten materials have around 1900 atoms. When the number of atoms in the computational layer is below 100, the materials can be regarded as ablated out and gas phase materials. The total quantity of the plume and the material ablation rate are strongly influenced by the laser fluence. After 40 ns when laser heating stops, little plume is ejected from the surface of the irradiated target for all laser fluencies. Compared with other laser fluences, the quantity of the plume at laser fluence of 20 J/m^2 presents a sharp rise at 10 ns. The direct reason for this dramatic increase is that the ejected plum is composed of not only evaporated molecules but also liquid clusters. In order to capture the stepwise change clearly, the rate of material removal is given in Fig. 7(b). The rate of material removal is calculated by taking the time derivative of the material removal shown in Fig. 7(a). The abrupt change in Fig. 7(a) is clearly indicated as a jump of the ablation rate in Fig. 7(b). The ablation rate at laser fluence 20 J/m^2 is up to 12,000/ns, which is much larger than that of other laser fluencies. This strong change of the ablation rate indicates the occurrence of phase explosion in nanosecond laser–material interaction, although this explosion only lasts a short time. In addition to the sudden ablation rate increase, phase explosion also features strong volume phase change. When the laser fluence is

Author's personal copy

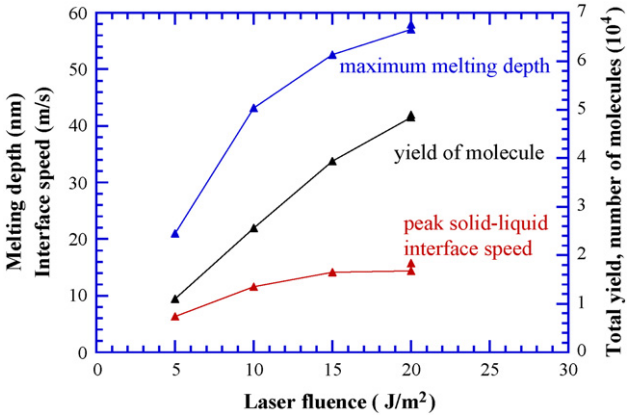

Fig. 8. The maximum melting depth, yield of molecules, and peak speed of the solid–liquid interface at different laser fluences.

higher than the phase explosion threshold, the ablation process turns the melt into a mixture of liquid and vapor. Detailed description can be found in Xu's work [26].

Fig. 8 shows the maximum melting depth, yield of molecules (ablation) and peak moving speed of the solid–liquid interface as a function of the laser fluence. At 20 J/m^2, the peak solid–liquid interface speed reaches a plateau while the melting depth and yield of molecules still show strong increase with the laser fluence. It is observed that for the laser fluences studied in this work, the yield of molecules has a nearly linear relationship with the laser fluence. Such relationship indicates weak phase explosion during laser–material interaction. If phase explosion takes place, it is expected a jump in the yield of molecules will be observed since phase explosion is anticipated to remove materials more intensively.

4. Conclusion

In this work, large-scale hybrid atomistic-macroscale simulation was conducted to study the long-time (up to 60 ns) laser interaction with argon crystal. The research was focused on the long-time fundamental physics and phase change phenomena. Full solidification/epitaxial re-growth was observed within the time of 60 ns for the laser fluence of 5 J/m^2. No visible super-heating was observed at the solid–liquid interface which is very different from picosecond laser–material interaction. Study of the effect of the laser fluence shows that when the laser fluence is higher, the melting tends to stop later, and a higher peak melting speed will appear. For the laser fluences studied in this work, an almost linear relationship was observed between the ablation yield and the laser fluence, indicating weak phase explosion.

Acknowledgements

Support from the start-up fund of Iowa State University is gratefully acknowledged. Partial support of this work from NSF (CMS: 0457471), Air Force Office for Scientific Research and MURI from ONR is gratefully acknowledged.

References

[1] M. Shibahara, S. Kotake, Int. J. Heat Mass Transfer 40 (1997) 3209.
[2] H. Hakkinen, U. Landman, Phys. Rev. Lett. 71 (1993) 1023.
[3] S. Kotake, M. Kuroki, Int. J. Heat Mass Transfer 36 (1993) 2061.
[4] R. Herrmann, J. Gerlach, E.E.B. Campbell, Appl. Phys. A 66 (1998) 35.
[5] L. Zhigilei, P. Kodali, B. Garrison, J. Phys. Chem. B 101 (1997) 2028.
[6] L. Zhigilei, P. Kodali, B. Gassison, J. Phys. Chem. B 102 (1998) 2845.
[7] L. Zhigilei, B. Garrison, J. Appl. Phys. 88 (2000) 1281.
[8] E. Ohmura, I. Fukumoto, in: Proceedings of the International Congress on Applications of Lasers and Electro-Optics, 219, 1999.
[9] D. Ivanov, L. Zhigilei, Appl. Phys. A 79 (2004) 977.
[10] D. Ivanov, L. Zhigilei, Phys. Rev. B 68 (2003) 22.
[11] M. Zeifman, B. Garrison, L. Zhigilei, in: Proceedings of the 23rd International Symposium of AIP Conference, 663, 2003, p. 939.
[12] J. Etcheverry, M. Mesaros, Phys. Rev. B 60 (1999) 9430.
[13] X. Xu, C. Cheng, I. Chowdhury, J. Heat Transfer 126 (2004) 727.
[14] X. Xu, D. Willis, J. Heat Transfer 124 (2002) 293.
[15] L. Zhigilei, Appl. Phys. A 76 (2003) 339.
[16] L. Zhigilei, J. Phys. 59 (2007) 413.
[17] L. Zhigilei, Phys. Rev. Lett. 91 (2003) 105701.
[18] L. Zhigilei, Appl. Surf. Sci. 248 (2005) 433.
[19] L. Zhigilei, B. Garrison, Mater. Res. Soc. Symp. Proc. 538 (1999) 491.
[20] M. Allen, D. Tildesley, Computer Simulation of Liquids, Clarendon Press, Oxford, 1987.
[21] X. Wang, Y. Lu, J. Appl. Phys. 98 (2005) 114304.
[22] X. Wang, X. Xu, J. Heat Transfer 124 (2002) 265.
[23] X. Wang, J. Phys. D: Appl. Phys. 38 (2005) 1805.
[24] X. Wang, X. Xu, Int. J. Heat Mass Transfer 46 (2003) 45.
[25] X. Wang, C. Lawrence, Proceedings of the 37th AIAA Thermophysics Conference, June 28–July 1, 2004, Portland, Oregon, 2004.
[26] X. Xu, Appl. Surf. Sci. 197-198 (2002) 61.